Engineering titania nanostructure to tune and improve its photocatalytic activity

Matteo Cargnello[a,b,c], Tiziano Montini[d], Sergey Y. Smolin[e], Jacqueline B. Priebe[f], Juan J. Delgado Jaén[g], Vicky V. T. Doan-Nguyen[h], Ian S. McKay[b,c], Jay A. Schwalbe[b,c], Marga-Martina Pohl[f], Thomas R. Gordon[a], Yupeng Lu[h], Jason B. Baxter[e], Angelika Brückner[f], Paolo Fornasiero[d], and Christopher B. Murray[a,h,1]

[a]Department of Chemistry, University of Pennsylvania, Philadelphia, PA 19104; [b]Department of Chemical Engineering, Stanford University, Stanford, CA 94305; [c]SUNCAT Center for Interface Science and Catalysis, Stanford University, Stanford, CA 94305; [d]Department of Chemical and Pharmaceutical Sciences, Institute of Chemistry of Organometallic Compounds, National Research Council (CNR), National Interuniversity Consortium of Materials Science and Technology (INSTM), University of Trieste, 34127 Trieste, Italy; [e]Department of Chemical and Biological Engineering, Drexel University, Philadelphia, PA 19104; [f]Leibniz-Institut für Katalyse e.V., Universität Rostock, 18059 Rostock, Germany; [g]Departamento de Ciencia de los Materiales e Ingeniería Metalúrgica y Química Inorgánica, Facultad de Ciencias, Universidad de Cádiz, 11510 Puerto Real, Spain; and [h]Department of Materials Science and Engineering, University of Pennsylvania, Philadelphia, PA 19104

Approved March 1, 2016.

Photocatalytic pathways could prove crucial to the sustainable production of fuels and chemicals required for a carbon-neutral society. Electron–hole recombination is a critical problem that has, so far, limited the efficiency of the most promising photocatalytic materials. Here, we show the efficacy of anisotropy in improving charge separation and thereby boosting the activity of a titania (TiO_2) photocatalytic system. Specifically, we show that H_2 production in uniform, one-dimensional brookite titania nanorods is highly enhanced by engineering their length. By using complimentary characterization techniques to separately probe excited electrons and holes, we link the high observed reaction rates to the anisotropic structure, which favors efficient carrier utilization. Quantum yield values for hydrogen production from ethanol, glycerol, and glucose as high as 65%, 35%, and 6%, respectively, demonstrate the promise and generality of this approach for improving the photoactivity of semiconducting nanostructures for a wide range of reacting systems.

titania | brookite | photocatalysis | photoreforming | hydrogen

Photocatalysis could play an important role in the new clean energy economy (1, 2). By using photoexcited electrons and holes to drive chemical reactions using absorbed sunlight, photocatalytic processes offer potential carbon-free means of both neutralizing waste and producing various fuels and chemicals (3). However, although photocatalysis is already used in niche industrial applications (4), the wider promise of photocatalytic processes at industrial scale has gone unrealized. A main reason for this failure is fast electron–hole recombination following light absorption in most photocatalysts (5). As a result, previous efforts at photocatalyst engineering have focused on charge separation efficiency (6). Heterojunctions can enhance charge separation by electron or hole transfer from one semiconductor to another (or to a metal) (7), provided that the correct energy band alignment is present. Other strategies can be used, for example by facet engineering (8), such that electrons and holes are driven toward different surfaces. The use of organic surfactants provides the opportunity to control the crystal phase and the exposed crystal facets (8, 9). Despite some advances, a clear path toward improvement in charge separation is still missing, resulting in quantum efficiencies that are still low, even in the best existing photocatalytic systems.

One of the most promising applications of heterogeneous photocatalysis is hydrogen production. Hydrogen is considered to be one of the potential energy vectors of the future, and its utilization in fuel cells represents a clean way to convert chemical into electrical energy (10). Currently, 95% of hydrogen is obtained from fossil fuels (mainly natural gas) by steam reforming in an unsustainable process (11). Given that hydrogen is also a commodity chemical used at the million-ton scale for several industrial processes (e.g., ammonia synthesis), methods that could sustainably produce hydrogen would represent a great economic and environmental benefit. Potential options are available, such as aqueous reforming of biomass (12), but they still require intense energy input. Photocatalytic reforming, in which light converts low-quality or low-purity biomass-derived compounds or waste streams into hydrogen, represents an alternative that can be nearly carbon-neutral, by using renewable resources and sunlight as the only feedstock (3).

Among semiconductors, titanium dioxide (TiO_2, titania) is the most studied and is therefore used as a benchmark photocatalytic material (13). Its stability, activity, and Earth abundance makes it the premier photocatalytic system. Anatase and rutile TiO_2 polymorphs have been thoroughly investigated because they are thermodynamically favored in the nanoscale form and in the bulk, respectively (14). Brookite, in contrast, has rarely been studied, despite theoretical and experimental data supporting its higher activity in some photocatalyzed transformations (15–20). Previously, structural modifications (21), doping (22), or the formation of heterojunctions with plasmonic building blocks (23) have shown promise in promoting its photocatalytic activity. However, these efforts leave much to be desired in boosting the charge-separating ability of TiO_2 to industrially viable levels.

Here, we demonstrate an approach to reduce recombination and improve the photoactivity of titania by tuning the structure

Significance

This work shows that hole–electron recombination can be controlled by engineering the length of brookite nanorods, and that a variety of organic substrates can be efficiently oxidized as the counterreaction to hydrogen evolution. Both are important steps to developing photocatalysis as a sustainable technology. Electron–hole recombination is a major fundamental limitation in any photocatalytic process. By controlling and reducing it with rod length, we can increase the efficiency of photocatalyzed processes. Also, by utilizing demanding substrates in aqueous media, ethanol, glucose, and glycerol, we make a step toward the photoreforming of more plentiful feedstocks such as, or derived from, biomass.

Author contributions: M.C., T.M., P.F., and C.B.M. designed research; M.C., T.M., S.Y.S., J.B.P., J.J.D.J., V.V.T.D.-N., I.S.M., J.A.S., M.-M.P., T.R.G., and Y.L. performed research; M.C., T.M., S.Y.S., J.B.P., I.S.M., and J.A.S. wrote the paper; J.B.B. supervised the ultrafast spectroscopy part; A.B. supervised the paramagnetic spectroscopy part; and P.F. and C.B.M. supervised the overall project.

The authors declare no conflict of interest.

[1]To whom correspondence should be addressed. Email: cbmurray@sas.upenn.edu.

of nanorods in the brookite phase. This method has a profound influence on the photocatalytic reforming activity of the system, and is used to demonstrate efficient hydrogen production from several low-purity, potentially biomass-derived compounds. By achieving exquisite control over the nanostructure and the electronic properties of the photocatalyst, we provide a paradigm for the preparation of highly active TiO_2 photocatalysts that could be implemented across the wide range of systems and substrates for which TiO_2 is already used.

Results and Discussion

Preparation and Characterization of Brookite Nanorods of Different Lengths. The synthesis of pure-phase brookite titania nanorods is based on a seed-mediated approach, which initially produces anatase seeds that are then grown into brookite rods by further injection of precursor (24). A large excess of oleylamine is required for the hydrolysis of the titanium chloride–oleic acid precursor, in accordance with other synthesis methods that show brookite being favored with a slow in situ production of OH^- ions (16). Anisotropic growth of the seeds is accomplished by decomposition and deposition of additional precursors during synthesis. Because the growth is achieved through slow injection, the length of the rods is easily tunable by controlling the volume of additional precursors. It has been observed that the nanorods switch from the anatase to the brookite phase when they grow to about 15 nm in length (24). In this work, five samples of brookite nanorods of different average lengths greater than 20 nm were prepared. Transmission electron microscopy (TEM) images of the samples are shown in Fig. 1 *A*–*E*. The samples show uniform (10–12% dispersion) and distinct lengths that vary from 25 nm to 45 nm (see histograms associated with Fig. 1 *A*–*E*). The samples are labeled as short, short-medium, medium, medium-long, and long with increasing length. Under the present experimental conditions, a growth rate of about 5 nm·mL^{-1} of added precursor was observed at the initial growth stages. Given that the diameter of the rods (~4–6 nm) does not vary drastically between samples, about 90% of the additional titanium precursor injected is decomposed on the surface of the rods and contributes to increasing their length. At later stages, however, the growth rate decreases due to the poor solubility of the longer rods in the reaction mixture, which leads to self-nucleation of nonuniform anatase particles. These by-products can be removed by careful size-selective purification, which also improves the length distribution of the samples. This procedure exploits the size-dependent solubility of the particles and is performed by adding an antisolvent (isopropanol) to the solution. The longer rods, being less soluble than smaller particles, precipitate first and are separated from the supernatant containing the particles by centrifugation and redissolved for further use.

The organic ligands on the rods can be removed by treatment with $NOBF_4$, which replaces the alkyl ligands with small BF_4^- ions, and provides samples that can be isolated, dried, and used as powders (25). Synchrotron X-ray diffraction (XRD) data of such powders (Fig. 1*F*) indicates the formation of pure-phase brookite rods, with relative intensities differing from the theoretical values and a general broadening due to microstrain and size dispersion. There are no clear features that can be associated with the elongation of the crystal structure, likely because of strain. Raman spectra (Fig. 1*G*) further corroborate the phase purity, with the plethora of peaks between 200 cm^{-1} and 600 cm^{-1} that are characteristic of the brookite structure (16, 24, 26). As observed in XRD patterns, broad signals preclude an accurate comparison between the samples, and no differences in peak position or breadth are distinguishable. A bandgap of 3.4 eV for all of the samples was measured using diffuse reflectance UV-visible (UV-Vis) spectroscopy (Fig. 1*H*). This value is larger than that of rutile and anatase polymorphs, and in accordance with previous works on brookite materials (16). Such a large bandgap and the associated cathodic shift of the conduction band are advantageous for photocatalytic hydrogen evolution.

Photocatalytic Activity for Alcohol Photoreforming. The nanorods were tested for photocatalytic hydrogen production from aqueous ethanol solutions under solar simulated irradiation, using an

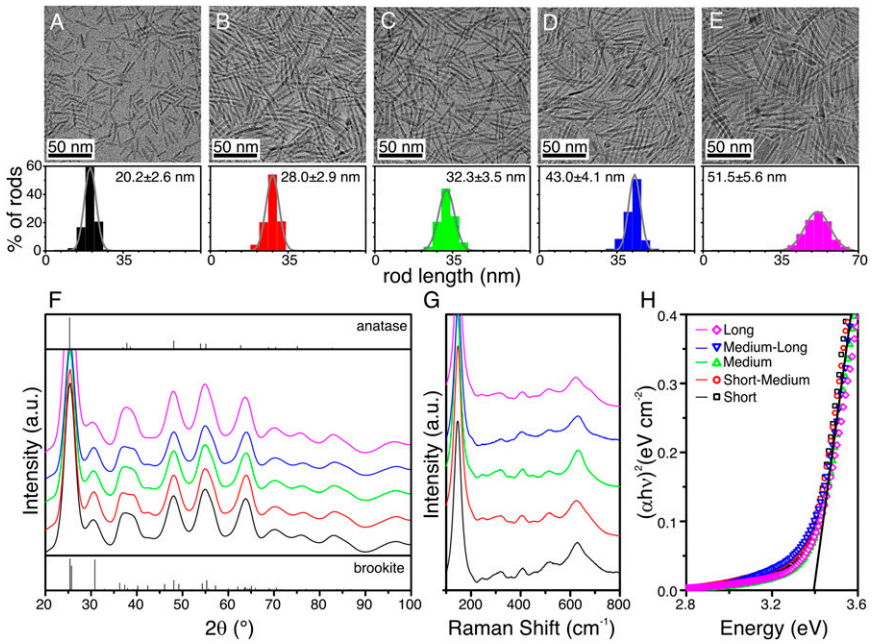

Fig. 1. Brookite nanorods of different lengths used in this work. (*A*–*E*) TEM images of short (*A*), short-medium (*B*), medium (*C*), medium-long (*D*), and long (*E*) brookite rods synthesized by a seed-mediated approach, with associated histograms of length distributions (bottom). (*F*) Synchrotron XRD patterns of the samples and reference patterns for pure anatase (top) and brookite (bottom). (*G*) Raman spectra using 532-nm laser excitation source. (*H*) Kubelka–Munk plot derived from diffuse reflectance UV-Vis spectroscopy experiments.

air mass 1.5 (AM1.5) filter with about 4% of the energy in the UV region (<400 nm). Instead of the often-studied methanol, which is mainly produced from fossil fuels (syngas), ethanol was selected as a model compound because it is obtained from biomass through fermentation of lignocellulosic-derived sugars (27) or from CO_2 by genetically engineered microbes (28). It therefore represents a sustainable source for H_2 production. In addition, ethanol oxidation requires breaking a C–C bond. This aspect makes it a better facsimile for more complicated feedstocks like biomass compared with methanol. To control the catalyst loading, the nanorods still coated with organic ligands were drop-casted from hexane–octane solutions onto cover glass slides to form thin films. The use of films is advantageous over powders and slurries because of the ease of recoverability and recyclability when considering realistic applications of these materials (29). To reduce the kinetic barrier for H_2 production (30), Pt was used as a standard cocatalyst, although nonnoble metals such as Cu can also be used (31). To avoid catalytic activity disparities because of Pt particle size differences using conventional impregnation or photodeposition methods, colloidal Pt nanocrystals with uniform particle size distributions of 4.5 ± 0.4 nm (Fig. S1) were codeposited with the nanorods using the same metal loading for all of the samples (1 wt %). Given that nanorods without Pt are not active for hydrogen production under these conditions, the low loading guarantees that the overall number of active Pt/nanorod pairs remain the same for all of the samples. Therefore, the same metal loading allows a fair comparison between samples with equally exposed metal surface area. The films were highly homogeneous and smooth, as demonstrated by scanning electron microscopy (SEM), with uniform thicknesses on the order of ~100 nm and clearly showing the presence of mesopores created by random stacking of the rods (see Fig. S2). All films were highly active for ethanol photoreforming, with H_2 evolution rates approaching 45 $mmol \cdot h^{-1} \cdot g^{-1}$ for the overall best performing sample, the medium nanorods (Fig. 2 *A* and *B*), and rates were highly repeatable and reproducible (see Fig. S3). This rate of hydrogen production under simulated solar irradiation is among the highest for titania-based photocatalysts (16, 21, 32). Furthermore, the rate of H_2 production of medium nanorods is 3 times that of the short nanorods (Fig. 2*B*). The delay in reaching steady-state hydrogen production was due to the removal of organic ligands from the surface of the nanorods, as demonstrated by infrared spectroscopy performed on the films before and after photocatalytic activity (see Fig. S4). Further proof was provided by experiments performed by recycling the films several consecutive times (see Fig. S5). During the second and third runs, there is a much lower delay in H_2 production related only to hydrogen detection by the system. Furthermore, the films were proven to provide stable hydrogen production for days. Following International Union of Pure and Applied Chemistry (IUPAC) recommendations (33), rates were normalized by specific surface area, which was measured using a recently developed method based on adsorption of Kr at liquid argon temperature (34, 35). The films are mesoporous and show high specific surface areas between 100 $m^2 \cdot g^{-1}$ and 250 $m^2 \cdot g^{-1}$, with narrow pore size distribution (see Fig. S6), confirming morphology apparent in SEM. Differences in surface area can be related to differences in the packing density of the rods in the films. After normalization, long rods were found to be the most active, with an intrinsic hydrogen production rate that was roughly 8 times that of short rods. The quantum yields for hydrogen production, i.e., the fraction of photons that are used in the chemical reaction to produce hydrogen, were measured in a separate experiment using monochromated light at 365 nm also following IUPAC recommendations (33). In the case of ethanol, quantum yields as high as 65% were calculated, which are among the highest reported for platinized titania materials (36). This value can be further increased by optimizing ethanol concentration, metal loading, or photoreactor design, which goes beyond the focus of this manuscript.

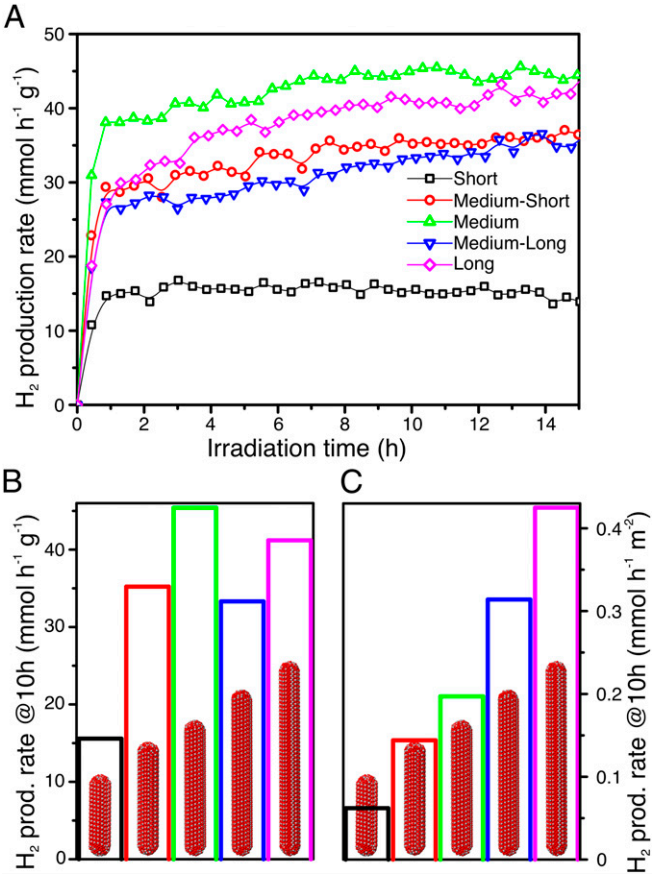

Fig. 2. Ethanol photoreforming on 1 wt % Pt–brookite nanorods of different length. (*A*) Rates of H_2 production over time. (*B*) Rates after 10 h under illumination normalized by weight of photocatalyst. (*C*) Rates after 10 h under illumination normalized by surface area of the photocatalysts.

The samples were also tested for photoreforming of more-challenging renewable alcohols, such as glycerol and glucose (see Fig. S7). In accordance with the higher complexity of these two polyalcohols, overall rates were lower than when using ethanol (3). However, these rates were still remarkable, and quantum yields of 35% and 6% for glycerol and glucose, respectively, were measured. Photocatalytic rates for glycerol still showed the long rods as performing best when the data were normalized by surface area, but, for glucose, the difference between the samples was noticeably smaller. It is likely that surface reactions and diffusion rates, rather than hole–electron separation, become limiting. One possibility is that the active sites are intrinsically less active for glucose oxidation. Another possibility is that glucose requires a different active site, perhaps the sterically unencumbered tips, and so the kinetics are limited by the number of active sites. Additionally, a delay in reaching steady-state rates is observed with glycerol. This delay is due to the removal of organic ligands from the surface of the rods, which takes longer than in ethanol because of the lower hole extraction rate for glycerol, or because of equilibria in solution that cause a delay in the detection of H_2. With glucose, a strong deactivation was also observed, suggesting poisoning of the catalyst/cocatalyst surface by by-products of the initial glucose oxidation steps. The trend is different compared with the other two compounds because the observed forward rates are decreased by deactivation phenomena.

Deactivation becomes more prominent as the reaction proceeds and more by-products are formed. Intermediate products of the photoreforming process are indeed known to potentially inhibit the reaction by blocking active sites (36, 37).

During photoreforming of ethanol, acetaldehyde and 1,1-diethoxyetane are produced by dehydrogenation and accumulated in the liquid phase (only traces amounts are removed from the solution by the inert gas flow). No CO_2 formation has been observed, confirming that ethanol is oxidized more readily than acetaldehyde. In the case of glycerol and glucose, CO_2 is detected as a by-product in the gas phase as a result of the oxidation/decarboxylation of the organic skeleton. This process is possible because intermediates following the initial dehydrogenation still contain OH groups. These intermediates can favorably compete with the initial substrate and bind to the surface of TiO_2 for further oxidation. In the case of glycerol, the analysis of the liquid phase revealed the presence of 1,3-dihydroxy-2-propanone, hydroxyacetaldehyde, and formic acid as major by-products, in agreement with previous reports on photoreforming of glycerol on TiO_2-based materials (37).

In-Depth Characterization Studies. Several techniques were used to shed light on the observed catalytic trends. High-resolution TEM investigations were carried out both before (see Fig. S8) and after catalytic activity (Fig. 3). The size and shape of both Pt nanocrystals and titania nanorods were maintained during photocatalysis, even after reaction for more than 20 h. The nanorods, despite unavoidable agglomeration in the solid state, also maintained their crystallinity, as evidenced by the lattice fringes in Fig. 3*A*. Analysis of digital diffraction patterns on multiple nanorods demonstrated that most of them were in the brookite phase, and only a small percentage (<5%) could be tentatively assigned to the anatase phase. It must be highlighted that, in a few cases, it was hard to clearly distinguish anatase from brookite, making the definitive assignment difficult. The results for the other samples were in line with those shown for the long rods. There was no preferential exposure of specific surface facets, in accordance with XRD results, ruling out differences in exposed facets as an explanation for the higher H_2 production rate of some samples (18).

We set out to investigate the behavior of electrons and holes under irradiation on the different samples using two complimentary techniques, electron paramagnetic resonance (EPR) spectroscopy and transient absorption (TA), probing electron and hole activity, respectively.

Fig. 4*A* shows EPR spectroscopy data at −173 °C on the ligand-exchanged samples under irradiation with UV-Vis light. Each spectrum could be deconvoluted by spectrum simulation into a combination of four signals (C1–C4, Fig. 4*D* and table in Fig. 4*E*, as in the example of the medium rods in Fig. 4 *B* and *C*). The isotropic signal C1 likely arises from organic residues still on the particle surface after ligand exchange, which can produce stable radicals upon photooxidation by the positive holes in UV-irradiated TiO_2 (38). C2 and C3 are most likely Ti^{3+} species of the brookite phase (39) formed by trapped UV-excited electrons at bulk (C2) or surface (C3) Ti^{4+} sites. C4 is assigned to $HO_2^{\bullet}$ radicals, which can arise from the reaction of holes with the surface hydroxyl groups on TiO_2 (40, 41). The contribution of each signal to the whole spectrum as derived by spectrum simulation is reported in Fig. 4*D*. For the least active sample (short rods), the relative intensity of signal C1 is lowest, whereas the total contribution of Ti^{3+} (C2 and C3) is highest. If photoexcited electrons were quickly transferred to the Pt particle, reducing electron–hole recombination, there would be no EPR signal. Therefore, a higher Ti^{3+} signal intensity in the short nanorod sample suggests a slower or inhibited transfer to Pt, agreeing with the observed lower activity (42). At the reaction temperature (room temperature), exciton recombination is likely to be even faster. Indeed, when ethanol is added at room temperature in the EPR tube for in situ experiments (Fig. 4*F*), the C1 signal decreases. This decrease is related to the preferential reaction of holes with ethanol, leaving the electron localized on a Ti^{3+} ion, and thus confirming that the C1 signal is a good indicator of the reactivity of the samples. In summary, the different intensities of the Ti^{3+} and C1 EPR signals as well as the behavior of the latter in the presence of ethanol indicate that the transfer of photoexcited electrons to Pt as well as the reaction of holes with ethanol is fastest for the most active sample, the long rods.

Ultrafast TA spectroscopy of the nanorod films was performed to quantify lifetimes of photoexcited carriers and complement EPR studies (43). Ultrafast measurements of Pt-decorated nanorod films were performed in situ with the same ethanol mixture that was used in the hydrogen evolution experiment. The

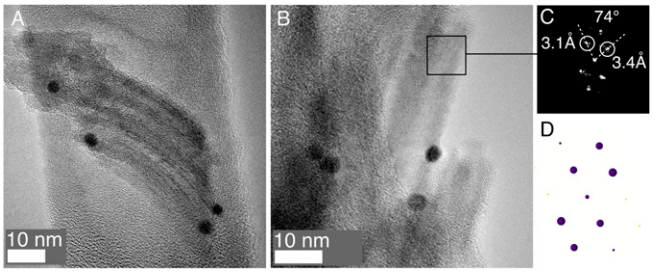

Fig. 3. High-resolution TEM characterization of long nanorods after photocatalytic activity. (*A* and *B*) Representative high-resolution (HR) TEM images. Black particles are Pt nanocrystals. (*C*) Digital diffraction pattern of a selected area, showing distances and angles for specific planes. (*D*) Simulated diffraction pattern for brookite phase viewed along the [2 1 3] zone axis, showing a very good match with the experimental pattern in *C*.

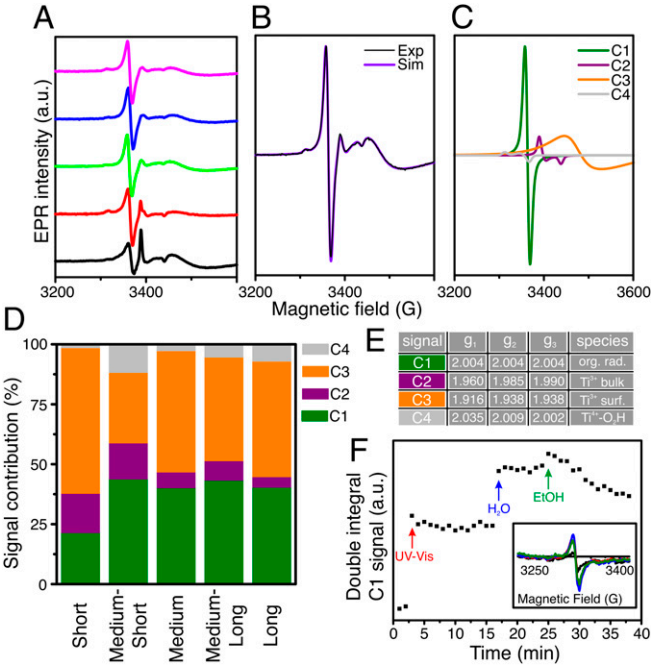

Fig. 4. EPR spectroscopy experiments. (*A*) EPR signals recorded at −173 °C. (*B*) Combined experimental and simulated EPR patterns, and (*C*) deconvolution of the EPR trace into its constituent signals according to literature reports. (*D*) Contribution of the four EPR-active signals to the total EPR trace. (*E*) EPR signal assignments. (*F*) In situ EPR experiment on the medium rods by switching from dark to UV-Vis illumination, then adding water and, finally, ethanol as indicated by the arrows.

films were photoexcited with a 50-fs UV (4.0 eV) pump pulse, and the relaxation of carriers was monitored with an ultrafast visible probe pulse (see *Supporting Information* for further details). In accordance with previous investigations on titania particles, a broad photoinduced absorption feature in the visible range is obtained when pumping above the brookite band gap (see Fig. S9) (44). This feature has previously been assigned to trapped holes that lie energetically within the band gap and physically on or near the surface of the TiO_2 nanoparticles (44, 45). Trapping of photoexcited holes occurs on the order of a few hundred femtoseconds, which results in an ultrafast rise in the TA signal following photoexcitation (46). Trapped holes then relax to deeper trap states over the next few hundred picoseconds, resulting in a blue shift of the spectral feature (see Fig. S9) (47). The feature decays as trapped holes recombine with electrons or react to oxidize an adsorbate. The normalized kinetics of the visible absorption feature for each film are shown in Fig. 5*A*. To quantify the differences in dynamics, the kinetics were fit with a biexponential decay model according to:

$$\frac{\Delta T}{|\Delta T_{MAX}|} = A_1 e^{-\frac{t}{\tau_1}} + A_2 e^{-\frac{t}{\tau_2}} \quad [1]$$

Fits to the data are shown in Fig. 5*A*, and time constants are shown in Fig. 5*B*. The fast and slow time constants τ_1 and τ_2 are on the order of 100 ps and 1 ns, respectively. Investigation of nanorods without Pt in ethanol exhibited much faster single-exponential decays with time constants of 10–40 ps, increasing with nanorod length (see Fig. S10). These dynamics indicate that the capture of electrons by Pt increases the lifetime of the charge-separated state and that lifetimes increase with nanorod length, in accordance with the fact that samples with no Pt do not show detectable H_2 production. The increase in the lifetime of trapped holes with nanorod length is attributed to the larger volume available to the electron to remain separated from the hole. These data are consistent with the EPR results that indicate that electrons in longer nanorods transfer to Pt faster than electrons in shorter nanorods. This fact decreases the probability of recombination and thus in turn increases lifetimes of trapped holes in longer rods. Even if electrons can transfer between rods, the larger volume available is still a crucial element to limit recombination in the longer rods. Photooxidation of ethanol by trapped holes has been reported to occur on the order of nanoseconds in anatase (46), and it therefore competes more favorably with recombination in longer nanorods, in which carrier lifetimes are longer. Hence, photocatalytic activity is expected to be better for longer rods, which is consistent with the hydrogen evolution results in Fig. 2.

The hole and electron diffusion lengths in titania are about 10 nm and several micrometers, respectively (48). The holes are effectively confined to the width of the nanorods, whereas electrons are free to move over the whole length, thanks to their 1D nature (49). Recombination and electrical conductivity are lower in brookite compared with anatase, which are positive attributes for photocatalysis (50). For these reasons, we correlate the high H_2 production rate of the long rods with the delocalization of electrons along their 1D structure, which favors electron–hole separation and carrier extraction by protons and the alcohol.

It should be noted that the overall photocatalytic activity for these samples was not optimized. For example, a smaller Pt particle size or a lower loading can result in increased rates. Nevertheless, the brookite nanorods that we reported still showed among the highest H_2 production rates from alcohol photoreforming. More generally, we validated an approach where, by controlling the photocatalyst 1D structure using colloidal methods, we were able to manipulate its photocatalytic and electronic properties, thereby providing a general scheme for improving the activity of photocatalytic materials.

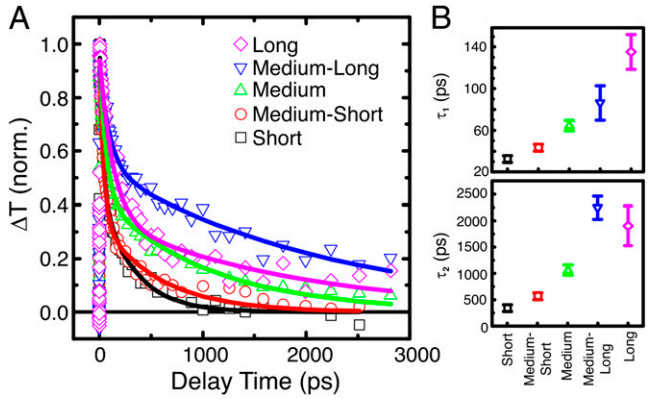

Fig. 5. In situ TA spectroscopy experiments. (*A*) Normalized TA kinetic traces of Pt-decorated nanorods in ethanol. Lines show fits with a biexponential model. (*B*) Fitted time constants [τ_1 (*Top*) and τ_2 (*Bottom*)] for brookite nanorod samples with Pt. Films were pumped at 4.0 eV at a fluence of 220 μJ·cm^{-2}. The broad absorption feature is integrated from 2.1 eV to 3.25 eV.

Conclusions

We demonstrated not only that brookite titania is a highly active phase for photocatalytic hydrogen generation but also that engineering its structure can lead to dramatic improvements of photocatalytic activity. We showed that the anisotropic, 1D nature of the photocatalyst allows a much improved electron–hole separation after light excitation. The result of these combined efforts are materials that show some of the highest rates and quantum efficiencies for hydrogen production from biomass-derived compounds. The manipulation of the exciton through crystal structure is not restricted to this particular set of materials but can be generally and widely applicable to other semiconductor-based nanostructures.

Methods

Nanorod Synthesis. Brookite nanorods were prepared using standard air-free Schlenk-type techniques following the synthesis described by Buonsanti et al. (24) with modifications to improve length control and particle dispersibility (8). See *Supporting Information* for further details.

Preparation of Photocatalytic Films. Pt nanocrystals of ~4.5 nm in size were prepared according to literature methods (51) and dissolved in hexanes to a concentration of ~5 mg Pt·mL^{-1}. Appropriate volumes of the two solutions were combined such that 1 mg of TiO_2 and 0.01 mg of Pt (1 wt %) were present, and the resulting solution was diluted with hexanes to a volume of 200 μL. Then, 50 μL of octane were added, and the solution was drop-casted onto cover glass slides (1.8 × 1.8 cm; Fisher Scientific). The slide was covered with a plastic lid to reduce the solvent evaporation rate, which was ~2 h. The samples were then used in the photocatalytic experiments without further treatment.

Photocatalytic Experiments. Photocatalytic activity was measured in a home-built photocatalytic reactor. The film was immersed in aqueous solutions of the sacrificial agent (1/1 by volume for ethanol, or 1 M glycerol or glucose). The sample was irradiated using a Solar Simulator equipped with a 150-W Xe lamp filtered with an atmospheric filter (AM1.5) to reduce the fraction of UV photons. Ar flow at a rate of 15 mL·min^{-1} was used to remove air from the reactor and to carry gaseous reaction products to the gas chromatograph. See *Supporting Information* for further details.

ACKNOWLEDGMENTS. Benjamin T. Diroll (University of Pennsylvania) is acknowledged for building the titania model in Fig. 2 and for discussions. C.B.M. and J.B.B. acknowledge support from a collaborative National Science Foundation (NSF) Grant (NSF CBET-1335821 to C.B.M. and NSF CBET-1333649 to J.B.B.). S.Y.S. and J.B.B. acknowledge further support from NSF ECCS-1201957. The ultrafast spectrometer at Drexel University was acquired

with funds from NSF MRI Award DMR-0922929. M.C. acknowledges partial support from NSF through the Nano/Bio Interface Center at the University of Pennsylvania, Grant DMR08-32802. J.J.D.J. is grateful for support to the Ramon y Cajal program and the Ce-NanoSurPhases project grant from MINECO. T.M. and P.F. acknowledge support from the Ministero dell'Istruzione, Università e Ricerca (Project 2010N3T9M4 "HI-PHUTURE"), EU FP7 COST Action CM1104 "Reducible oxide chemistry, structure and functions", National Interuniversity Consortium of Materials Science and Technology (INSTM), and University of Trieste (FRA2013 Project). Work at Beam Line 11-ID-B (GUP-32747) of the Advanced Photon Source, an Office of Science User Facility operated for the US Department of Energy (DOE) Office of Science by Argonne National Laboratory, was supported by the US DOE under Contract DE-AC02-06CH11357. I.S.M. was supported by the Department of Defense through the National Defense Science & Engineering Graduate Fellowship Program, and by the Fannie and John Hertz Foundation through a Hertz Foundation Fellowship. J.A.S. acknowledges support of the Stanford University Center for Interface Science and Catalysis (SUNCAT) seed funding from the Dean of Engineering and the Dean of Research at Stanford University. C.B.M. is grateful for the support of the Richard Perry University Professorship.

1. Kamat PV (2007) Meeting the clean energy demand: Nanostructure architectures for solar energy conversion. *J Phys Chem C* 111(7):2834–2860.
2. Lewis NS, Nocera DG (2006) Powering the planet: Chemical challenges in solar energy utilization. *Proc Natl Acad Sci USA* 103(43):15729–15735.
3. Cargnello M, et al. (2011) Photocatalytic H_2 and added-value by-products: The role of metal oxide systems in their synthesis from oxygenates. *Eur J Inorg Chem* 2011(28): 4309–4323.
4. Malato S, Blanco J, Vidal A, Richter C (2002) Photocatalysis with solar energy at a pilot-plant scale: An overview. *Appl Catal B* 37(1):1–15.
5. Schneider J, et al. (2014) Understanding TiO_2 photocatalysis: Mechanisms and materials. *Chem Rev* 114(19):9919–9986.
6. Colombo DP, Bowman RM (1996) Does interfacial charge transfer compete with charge carrier recombination? A femtosecond diffuse reflectance investigation of TiO_2 nanoparticles. *J Phys Chem* 100(47):18445–18449.
7. Zhang Z, Yates JT, Jr (2012) Band bending in semiconductors: Chemical and physical consequences at surfaces and interfaces. *Chem Rev* 112(10):5520–5551.
8. Gordon TR, et al. (2012) Nonaqueous synthesis of TiO_2 nanocrystals using TiF_4 to engineer morphology, oxygen vacancy concentration, and photocatalytic activity. *J Am Chem Soc* 134(15):6751–6761.
9. Jun YW, et al. (2003) Surfactant-assisted elimination of a high energy facet as a means of controlling the shapes of TiO_2 nanocrystals. *J Am Chem Soc* 125(51):15981–15985.
10. Dunn S (2002) Hydrogen futures: Toward a sustainable energy system. *Int J Hydrogen Energy* 27(3):235–264.
11. Holladay JD, Hu J, King DL, Wang Y (2009) An overview of hydrogen production technologies. *Catal Today* 139(4):244–260.
12. Cortright RD, Davda RR, Dumesic JA (2002) Hydrogen from catalytic reforming of biomass-derived hydrocarbons in liquid water. *Nature* 418(6901):964–967.
13. Chen X, Selloni A (2014) Introduction: Titanium dioxide (TiO_2) nanomaterials. *Chem Rev* 114(19):9281–9282.
14. Zhang H, Banfield JF (1998) Thermodynamic analysis of phase stability of nanocrystalline titania. *J Mater Chem* 8(9):2073–2076.
15. Kandiel TA, Robben L, Alkaim A, Bahnemann D (2013) Brookite versus anatase TiO_2 photocatalysts: Phase transformations and photocatalytic activities. *Photochem Photobiol Sci* 12(4):602–609.
16. Kandiel TA, et al. (2010) Tailored titanium dioxide nanomaterials: Anatase nanoparticles and brookite nanorods as highly active photocatalysts. *Chem Mater* 22(6): 2050–2060.
17. Li Z, Cong S, Xu Y (2014) Brookite vs anatase TiO_2 in the photocatalytic activity for organic degradation in water. *ACS Catal* 4(9):3273–3280.
18. Lin H, et al. (2012) Synthesis of high-quality brookite TiO_2 single-crystalline nanosheets with specific facets exposed: Tuning catalysts from inert to highly reactive. *J Am Chem Soc* 134(20):8328–8331.
19. Altomare M, et al. (2015) High activity of brookite TiO_2 nanoparticles in the photocatalytic abatement of ammonia in water. *Catal Today* 252(1):184–189.
20. Chiarello GL, Di Paola A, Palmisano L, Selli E (2011) Effect of titanium dioxide crystalline structure on the photocatalytic production of hydrogen. *Photochem Photobiol Sci* 10(3):355–360.
21. Chen X, Liu L, Yu PY, Mao SS (2011) Increasing solar absorption for photocatalysis with black hydrogenated titanium dioxide nanocrystals. *Science* 331(6018):746–750.
22. Asahi R, Morikawa T, Ohwaki T, Aoki K, Taga Y (2001) Visible-light photocatalysis in nitrogen-doped titanium oxides. *Science* 293(5528):269–271.
23. Linic S, Christopher P, Ingram DB (2011) Plasmonic-metal nanostructures for efficient conversion of solar to chemical energy. *Nat Mater* 10(12):911–921.
24. Buonsanti R, et al. (2008) Nonhydrolytic synthesis of high-quality anisotropically shaped brookite TiO_2 nanocrystals. *J Am Chem Soc* 130(33):11223–11233.
25. Dong A, et al. (2011) A generalized ligand-exchange strategy enabling sequential surface functionalization of colloidal nanocrystals. *J Am Chem Soc* 133(4):998–1006.
26. Tompsett GA, et al. (1995) The Raman spectrum of brookite, TiO_2 (Pbca, Z = 8). *J Raman Spectrosc* 26(1):57–62.
27. Hahn-Hägerdal B, Galbe M, Gorwa-Grauslund MF, Lidén G, Zacchi G (2006) Bio-ethanol—The fuel of tomorrow from the residues of today. *Trends Biotechnol* 24(12):549–556.
28. Gao Z, et al. (2012) Photosynthetic production of ethanol from carbon dioxide in genetically engineered cyanobacteria. *Energy Environ Sci* 5(12):9857–9865.
29. Gaya UI, Abdullah AH (2008) Heterogeneous photocatalytic degradation of organic contaminants over titanium dioxide: A review of fundamentals, progress and problems. *J Photochem Photobiol C Photochem Rev* 9(1):1–12.
30. Disdier J, Herrmann JM, Pichat P (1983) Platinum/titanium dioxide catalysts. A photoconductivity study of electron transfer from the ultraviolet-illuminated support to the metal and of the influence of hydrogen. *J Chem Soc Faraday Trans* 79(3):651–660.
31. Gombac V, et al. (2010) $CuO_{(x)}$-TiO_2 photocatalysts for H_2 production from ethanol and glycerol solutions. *J Phys Chem A* 114(11):3916–3925.
32. Chen X, Shen S, Guo L, Mao SS (2010) Semiconductor-based photocatalytic hydrogen generation. *Chem Rev* 110(11):6503–6570.
33. Braslavsky SE, et al. (2011) Glossary of terms used in photocatalysis and radiation catalysis (IUPAC recommendations 2011). *Pure Appl Chem* 83(4):931–1014.
34. Krause KM, Thommes M, Brett MJ (2011) Pore analysis of obliquely deposited nanostructures by krypton gas adsorption at 87 K. *Microporous Mesoporous Mater* 143(1):166–173.
35. Thommes M, Nishiyama N, Tanaka S (2007) Aspects of a novel method for the pore size analysis of thin silica films based on krypton adsorption at liquid argon temperature (87.3 K). *Stud Surf Sci Catal* 165(1):551–554.
36. Kondarides DM, Daskalaki VM, Patsoura A, Verykios XE (2008) Hydrogen production by photo-induced reforming of biomass components and derivatives at ambient conditions. *Catal Lett* 122(1):26–32.
37. Montini T, et al. (2011) Nanostructured Cu/TiO_2 photocatalysts for H_2 production from ethanol and glycerol aqueous solutions. *ChemCatChem* 3(3):574–577.
38. Cybula A, et al. (2014) The effect of calcination temperature on structure and photocatalytic properties of Au/Pd nanoparticles supported on TiO_2. *Appl Catal B* 152-153(1):202–211.
39. Livraghi S, et al. (2014) Nature of reduced states in titanium dioxide as monitored by electron paramagnetic resonance. II: Rutile and brookite cases. *J Phys Chem C* 118(38): 22141–22148.
40. Coronado JM, et al. (2001) EPR Study of the surface characteristics of nanostructured TiO_2 under UV irradiation. *Langmuir* 17(17):5368–5374.
41. Anpo M, et al. (1999) Generation of superoxide ions at oxide surfaces. *Top Catal* 8(3-4):189–198.
42. Naldoni A, et al. (2013) Pt and Au/TiO_2 photocatalysts for methanol reforming: Role of metal nanoparticles in tuning charge trapping properties and photoefficiency. *Appl Catal B* 130-131(1):239–248.
43. Baxter JB, Richter C, Schmuttenmaer CA (2014) Ultrafast carrier dynamics in nanostructures for solar fuels. *Annu Rev Phys Chem* 65(1):423–447.
44. Yoshihara T, et al. (2004) Identification of reactive species in photoexcited nanocrystalline TiO_2 films by wide-wavelength-range (400−2500 nm) transient absorption spectroscopy. *J Phys Chem B* 108(12):3817–3823.
45. Henderson MA (2011) A surface science perspective on photocatalysis. *Surf Sci Rep* 66(6-7):185–297.
46. Tamaki Y, et al. (2006) Direct observation of reactive trapped holes in TiO_2 undergoing photocatalytic oxidation of adsorbed alcohols: Evaluation of the reaction rates and yields. *J Am Chem Soc* 128(2):416–417.
47. Tamaki Y, et al. (2006) Trapping dynamics of electrons and holes in a nanocrystalline TiO_2 film revealed by femtosecond visible/near-infrared transient absorption spectroscopy. *C R Chim* 9(2):268–274.
48. Fisher AC, et al. (2000) Intensity dependence of the back reaction and transport of electrons in dye-sensitized nanocrystalline TiO_2 solar cells. *J Phys Chem B* 104(5): 949–958.
49. Varghese OK, Paulose M, Grimes CA (2009) Long vertically aligned titania nanotubes on transparent conducting oxide for highly efficient solar cells. *Nat Nanotechnol* 4(9): 592–597.
50. Kusumawati Y, et al. (2014) Charge transport and recombination in TiO_2 brookite-based photoelectrodes. *J Phys Chem C* 118(41):23459–23467.
51. Cargnello M, et al. (2013) Control of metal nanocrystal size reveals metal-support interface role for ceria catalysts. *Science* 341(6147):771–773.